

Grain boundaries amplify local chemical ordering in CrCoNi

Ian Geiger ¹, Yuan Tian ², Ying Han ², Yutong Bi ², Xiaoqing Pan ², Penghui Cao ^{2,3}, Timothy J. Rupert ^{1,2,4,5,*}

¹ Materials and Manufacturing Technology, University of California, Irvine, CA 92697, USA

² Department of Materials Science and Engineering, University of California, Irvine, CA 92697, USA

³ Department of Mechanical and Aerospace Engineering, University of California, Irvine, CA 92697, USA

⁴ Hopkins Extreme Materials Institute, Johns Hopkins University, Baltimore, MD 21218, USA

⁵ Department of Materials Science and Engineering, Johns Hopkins University, Baltimore, MD 21218, USA

* Corresponding author: tim.rupert@jhu.edu

ABSTRACT

Local chemical ordering plays an important role in the behavior of complex concentrated alloys, yet its characterization remains challenging due to the nanoscale dimensions and scattered spatial distribution of the ordered domains. This study explores the potential of grain boundaries as microstructural anchor points that amplify chemical ordering and enable the formation of compositional nanopatterns in CrCoNi. Using hybrid Monte Carlo/molecular dynamics simulations, we reveal the development of distinct compositional waves with ordering vectors normal to grain boundaries, extending to lengths greater than 6 nm. These waves manifest as periodic enrichment and depletion patterns, with strong Ni depletion near the Ni-segregated grain boundary accompanied by Co and Cr enrichment. Analogous to surface-driven phase separation,

the concentration waves emanating from the boundaries gradually attenuate as they propagate into the grain interior. This behavior highlights the interplay between boundary-dictated directional ordering and the isotropic, untemplated domain growth within the grain. This work advances our fundamental understanding of grain boundary-mediated ordering phenomena and offers a pathway for more precise experimental characterization of local chemical ordering in CCAs.

Keywords: Atomistic simulations, grain boundary segregation, chemical short-range order, high entropy alloy, local chemical order

I. Introduction

Complex concentrated alloys (CCAs) are a novel class of alloys formed by mixing three or more elements in roughly equimolar proportions [1]. A salient feature of these alloys is the complex chemical interactions that shape the atomic configurations and roughen the energy landscape. In CCAs with strongly interacting elements, characterized by the magnitude of the heat of mixing, selective bonding or repulsion between species can drive the formation of nanoscale chemical domains typically referred to as local chemical ordering (LCO) [2]. LCO can be further categorized by scale: chemical short-range order (CSRO) encompasses correlations within a few coordination shells (<1 nm) [3–5], while chemical medium-range order describes the extension of these correlations over larger distances (~ 1 -5 nm) [6]. Unlike long-range order with periodic atomic structures, LCO creates a rugged potential energy surface that influences the energetics and diffusion pathways of atomic-scale defects such as vacancies [7–9], dislocations [4,10,11], and grain boundaries [8,12–14]. For example, dislocations in CCAs can adopt wavy morphologies due to heterogeneous local atomic environments that pin or impede their motion, enhancing mechanical performance [15–17]. At grain boundaries, complex segregation states, sometimes driven by co-segregation [18,19], modify interfacial structures and properties. This can affect structural transformation pathways [14,20,21], suppress grain growth [22–25], and promote second-phase nucleation [25]. The diverse grain boundary structures and compositional variants in CCAs make these behaviors challenging to predict, highlighting the need for a deeper understanding of the mechanisms driving chemical order at grain boundaries.

To explore the vast configurational space in CCAs, accurate methods are needed to efficiently probe their thermodynamic and structural properties at the atomic scale. Atomistic simulations are ideal for this, as they provide spatial and chemical correlations on the relevant

length scales for LCO. For example, spin-polarized density functional theory (DFT) calculations have shown that frustrated magnetic alignments in CrCoNi minimize like-spin Cr bonds [26], corroborating extended X-ray absorption fine structure (EXAFS) [27] analyses that reveal preferential Cr-Ni and Cr-Co bonding. Alternatively, hybrid Monte Carlo (MC)/molecular dynamics (MD) simulations are well-suited for studying large systems across various time, temperature, and compositional domains, capturing the effect of compositional complexity on microstructural evolution mechanisms such as twinning [28], phase transformations [29], and grain boundary state transitions [14,20]. MC/MD simulations have been used to explore chemical order transitions in both face-centered cubic (FCC) [15,30] and body-centered cubic (BCC) CCAs [31–33], showing that lower temperatures generally increase the degree of LCO. Furthermore, chemical pair correlations are often enhanced near defects due to segregation [13,32,34], linking structural disorder with concentrated chemical ordering.

At the same time, experimental identification of LCO in CCAs remains highly challenging, largely due to the exceedingly small size of chemical clusters. These features often have domain widths on the order of a nanometer, making characterization difficult within the crystalline matrix. Advanced transmission electron microscopy (TEM) techniques offer key insights, with selected area electron diffraction (SAED) patterns showing extra superlattice reflections as a prevalent signature of LCO [35]. Streaking and diffuse discs at non-Bragg spots in reciprocal space further suggest spatial ordering under appropriate zone-axis conditions [4,35–39]. For example, nanobeam diffraction has identified extra diffuse disks at $\frac{1}{2}\{\bar{3}11\}$ positions along the [112] zone axis, proposed as evidence of CSRO in VCoNi [4,40], CrCoNi [5], and Fe₅₀Mn₃₀Co₁₀Cr₁₀ [38]. Similarly, diffuse scattering at $\frac{1}{3}\{\bar{4}22\}$ and $\frac{2}{3}\{\bar{4}22\}$ positions along the [111] zone axis in VCoNi [40] supports this interpretation. However, the origins of these reflections remain a subject of

debate [41–43], as similar features are observed in pure metals [44] and can also result from structural imperfections [45]. Moreover, scattering between reciprocal lattice planes from higher-order Laue zone diffraction can produce diffuse features unrelated to local composition along specific zone axes (e.g., $[\bar{1}1\bar{1}]$) [42,44]. This ongoing debate highlights inconsistencies in processing and characterization methodologies and emphasizes the gap between computational and experimental evidence of LCO.

To address this gap, new strategies for predictably localizing LCO within microstructures should be explored. Grain boundaries are promising in this context, as their structure and composition have been shown to drive other types of chemical transitions in nearby regions. For example, coherency stress energy associated with phase separation can be relieved at grain boundaries and surfaces [46,47], making these defects natural pinning centers for concentration waves. Extensive phase-field studies of spinodal decomposition in polycrystalline models show that attenuating concentration bands form parallel to interfaces due to segregation, driven by a balance between grain boundary-assisted phase separation and normal spinodal decomposition within the grain [46,48,49]. The high internal stresses in some CCAs, caused by LCO-related symmetry disruption and complex sublattice occupation [50–52], suggest that similar mechanisms may be active in CCAs with strong alloy interactions and lattice mismatch between ordered structures. These stresses become more significant when accounting for the diverse multi-stage phase separation pathways in CCAs [53], which are undoubtedly biased by the presence of defects.

In this work, atomistic simulations are used to investigate LCO and compositional patterning in the near-boundary regions of a $\Sigma 11$ $(332)\langle 110 \rangle$ symmetric tilt grain boundary in equiatomic FCC CrCoNi. This alloy is known for its strong ordering tendencies [5,36,54], with Han et al. [55] recently showing that LCO formation remains relatively insensitive to cooling rates

and annealing treatments. Moreover, the significant lattice strain accumulated during LCO formation [50] raises further questions about how interfacial structural relaxation influences local compositional morphology. Using bicrystal models, our hybrid MC/MD simulations reveal simultaneous bulk chemical ordering and grain boundary segregation, with Ni enrichment at the interface at low temperatures. Near-boundary compositional profiles show that compositional patterning can extend to widths of over 6 nm, where the Ni depletion is accompanied by this increased nanoscale ordering adjacent to the boundary. Spatial and chemical analysis indicates strong localization of Co-Cr chemical ordering in this region. Surprisingly, this segregation pattern persists even at high temperatures (up to 900 K), indicating a robust thermodynamic driving force, stemming from the grain boundary, that counters the typical chemical disordering expected at these temperatures. These results provide insights into potential pathways for isolating LCO in future experimental studies.

II. Computational Methods

An embedded atom method (EAM) potential developed by Li et. al. [15] was primarily used to model atomic interactions in the CrCoNi system. This potential has been previously characterized in-depth [15] and widely applied to study the effect of configurational state on defect evolution such as dislocations [15,28] and grain boundaries [14,56]. Special attention was given to adequately capturing the mixing enthalpies governing LCO formation during potential development. However, discrepancies in chemical correlations relative to DFT calculations [57–59] do exist. For example, while the EAM potential predicts less Ni-Cr ordering compared to DFT, both methods consistently predict Co-Cr ordering and Cr-Cr repulsion. This difference may originate from the lack of spin polarization considerations in the DFT calculations used to fit the

EAM potential, a limitation of classical potential formalisms in large-scale simulations. To address these discrepancies, a second set of limited simulations were performed with a recently developed neural network potential [60,61] that was designed to more accurately capture the expected chemical ordering behaviors based on DFT calculations. Importantly, both potentials predict significant elemental ordering/clustering at grain boundaries, aligning with experimental observations in comparable FCC CCAs [18,19,62].

Atomistic simulations were performed using the Large-scale Atomic/Molecular Massively Parallel Simulator (LAMMPS) software package [63]. The OVITO [64] software was used for visualization and adaptive Common Neighbor Analysis (CNA) [65] was used to analyze structure and identify defect atoms. The $\Sigma 11$ (332) $\langle 110 \rangle$ symmetric tilt grain boundary was chosen for this study due to previous evidence of near-boundary segregation at this interface in other CCAs [66]. The 0 K equilibrium grain boundary configuration was identified using an iterative sampling process [67]. Each simulation cell contained 135,168 atoms with dimensions at 0 K of $L_x \sim 13$ nm, $L_y \sim 28$ nm, and $L_z \sim 4$ nm and periodic boundary conditions in all directions (Figure 1(a)). Initial samples were generated using elemental Ni followed by random replacement of Ni with Co and Cr to obtain an equiatomic composition.

Annealing of the random solid solution at each target temperature was performed for 50 ps in the isothermal-isobaric (NPT) ensemble with an MD timestep of 2.5 fs. Hybrid MC/MD simulations followed in the NPT ensemble using the variance-constrained semi-grand canonical ensemble (VC-SGC) [68], which efficiently addresses limitations in canonical and semi-grand canonical ensembles in studying precipitation and phase segregation. Chemical potential differences of $\Delta\mu_{\text{Ni-Co}} = 0.021$ eV and $\Delta\mu_{\text{Ni-Cr}} = -0.031$ [15] were held constant to maintain equiatomic compositions, with the variance parameter κ equal to 10^3 . Every 20 MD steps, one

MC step was performed based on the Metropolis criterion, with atom swaps attempted for one-quarter of the atoms. Interface concentrations and potential energy were monitored to evaluate chemical and structural convergence, as shown in Figures 1(b) and (d) for a sample at 500 K. While these parameters appeared stable after approximately 30,000 MC steps, their gradients (Figures 1(c) and (e)), calculated as a moving average over 5,000 steps, revealed significant fluctuations over longer simulation periods. The simulations were determined to have converged when the absolute value of the total potential energy gradient dropped below 6 meV step^{-1} (dotted lines in Fig. 1(e)). At this point, both the energy and grain boundary concentrations plateaued, exhibiting only minor fluctuations. As a final step, a conjugate-gradient energy minimization was performed to remove thermal vibrations and facilitate structural comparisons between samples.

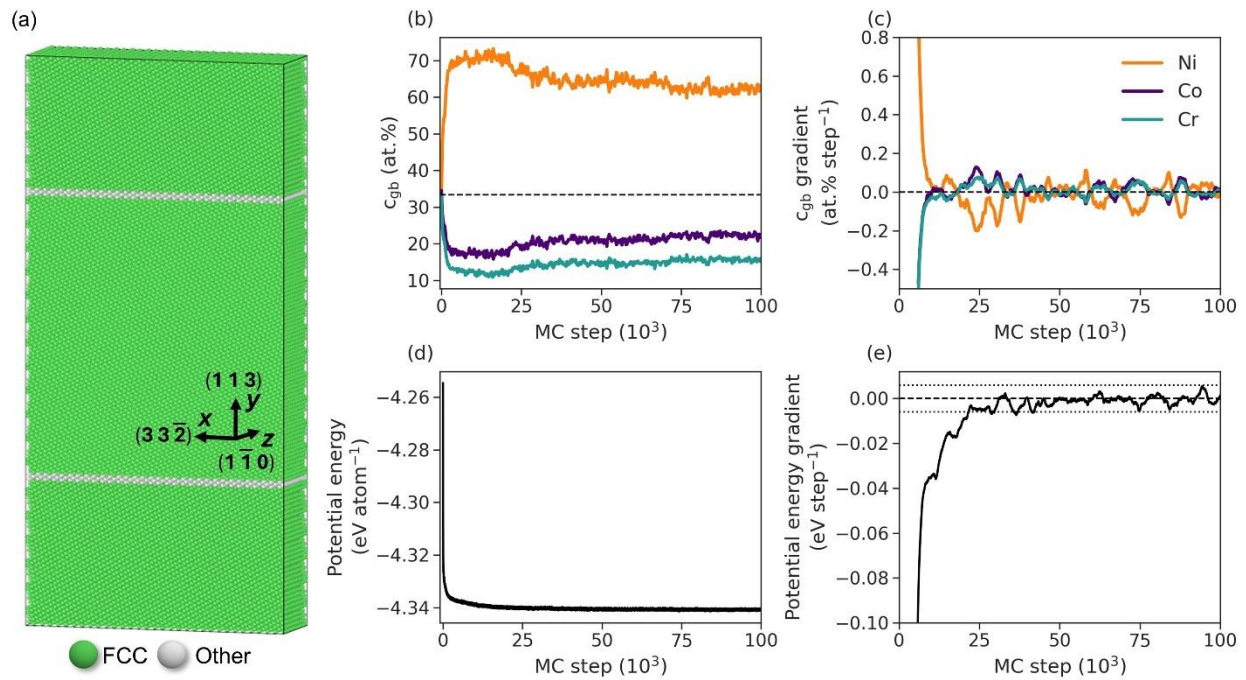


FIGURE 1. Atomistic model and convergence study. (a) A snapshot of the biocrystal with atoms colored by structure type, where green represents FCC atoms and white represents grain boundary atoms. (b) Grain boundary concentrations of each element plotted as a function of MC step at 500 K, and (c) the gradients of

each compositional slope taken over a 5,000 MC step window. (d) Potential energy per atom plotted by MC step, and (e) the respective gradient of potential energy with dotted lines denoting +/- 6 meV/step.

III. Results and Discussion

A. General segregation and ordering trends

Figure 2 shows the evolution of the grain boundary composition during the hybrid MC/MD simulations at 400 K, 600 K, and 800 K. Initially, all three interfaces begin with equiatomic concentrations (denoted by the black dashed line) but quickly become Ni-enriched and depleted in Cr and Co. It is worth noting that, at low temperatures, particularly 400 K, the Ni concentration quickly increases to around ~80% initially, followed by a gradual reduction to ~70%, highlighting the competition between grain boundary segregation and bulk chemical ordering. Ni is first attracted to the interface by structural driving forces, with high chemical disorder and minimal LCO in the bulk. As LCO develops within the grain, Ni redistribution into the crystalline regions becomes energetically favorable, contributing to cluster formation, similar to mechanisms driving suppressed surface segregation in strongly ordered alloys [69]. This effect is more pronounced at lower temperatures, resulting in longer convergence steps, about 2.5 times longer at 400 K than 600 K, and greater initial Ni segregation. In contrast, at 800 K, Ni segregation equilibrates rapidly, indicating that this competition is largely confined to lower temperatures.

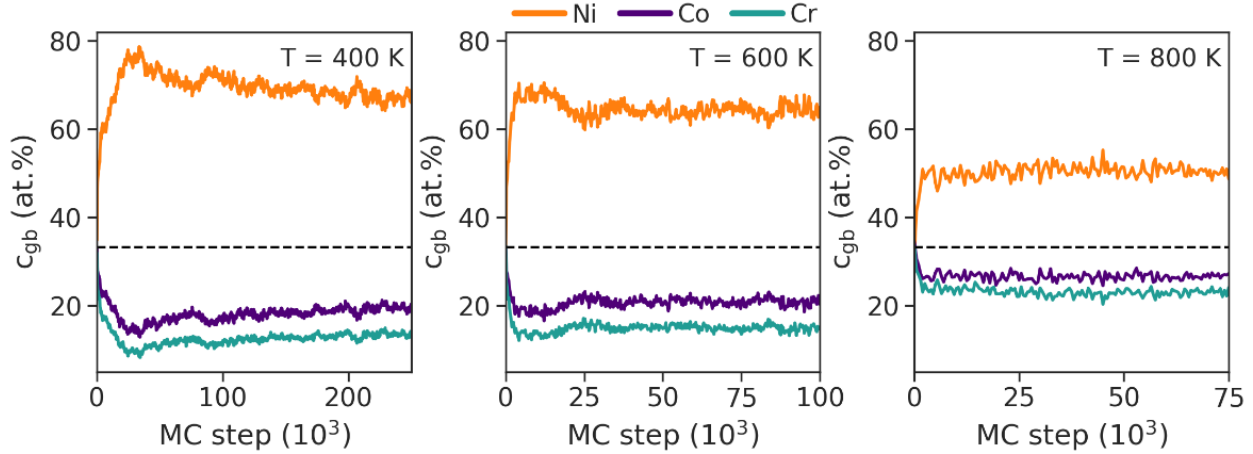


FIGURE 2. Grain boundary compositions as a function of the MC step at 400 K, 600 K, and 800 K, respectively.

Figure 3(a) shows the equilibrium grain boundary compositions for temperatures from 300 K to 1000 K (homologous temperatures T/T_m of ~ 0.17 to ~ 0.59 [70]). Here, the composition is averaged over the final 5000 MC steps, accounting for minor fluctuations in segregation (see Figure 2), represented by the error bars in Figure 3(a). Ni enrichment remains between 61% and 68% from 300 K to 700 K, then decreases towards equiatomic concentrations at higher temperatures. Co and Cr exhibit similar depletion rates. These trends are consistent with atom probe tomography analysis of FeMnNiCoCr alloys, which show Ni segregation and Cr depletion at low-angle and special high-angle boundaries aged at 450 °C [18]. Cao et al. [14] also predicted similar segregation for a high-angle $\Sigma 5$ boundary using the same EAM potential, with Ni enrichment exceeding 90 at.% at intermediate temperatures. The disparity in segregation magnitudes between that study and our results here can be explained by density-based thermodynamic models [18], which suggest that low-energy, high-density grain boundary structures (e.g., twin or $\Sigma 11$) offer weaker trapping environments for solute atoms compared to general high-angle boundaries.

Figure 3(b) shows the arrangement of solute species in defect sites at 400 K, viewed looking into the grain boundary plane. Ni (orange) atoms form distinct clusters, separated from the mixed Co (purple) and Cr (green) atoms. This pattern resembles spinodal-like decomposition seen in FeMnNiCoCr [19] and Fe-Mn [71], highlighting the influence of neighbor interactions and co-segregation over site-specific relaxation. To quantify such ordering in the bulk, the Warren-Cowley order parameter [72] is commonly used [7,15,30]. In its standard form, local atomic concentrations are compared to global concentrations to describe element pair ordering within a defined range. However, this method becomes problematic when applied to grain boundaries, where compositions often deviate significantly from global concentrations due to segregation. To address this, a modified grain boundary order parameter can be defined as:

$$\alpha_{n,GB}^{ij} = 1 - \frac{p_n^{j,i}}{c_{j,GB}}. \quad (1)$$

In Equation (1), $\alpha_{n,GB}^{ij}$ quantifies the interaction between a central grain boundary atom of species i and its neighboring atoms of species j in the n th neighbor shell. In this shell, $p_n^{j,i}$ represents the local concentration of species j around species i , while $c_{j,GB}$ is the concentration of species j in both grain boundary and neighboring crystalline sites within the n th shell of grain boundary atoms, calibrated for each temperature to account for variations in segregation state. In the absence of preferential ordering, $\alpha_{n,GB}^{ij}$ will be zero. Negative α_n^{ij} values indicate strong attractive interactions while positive values indicate repulsive interactions.

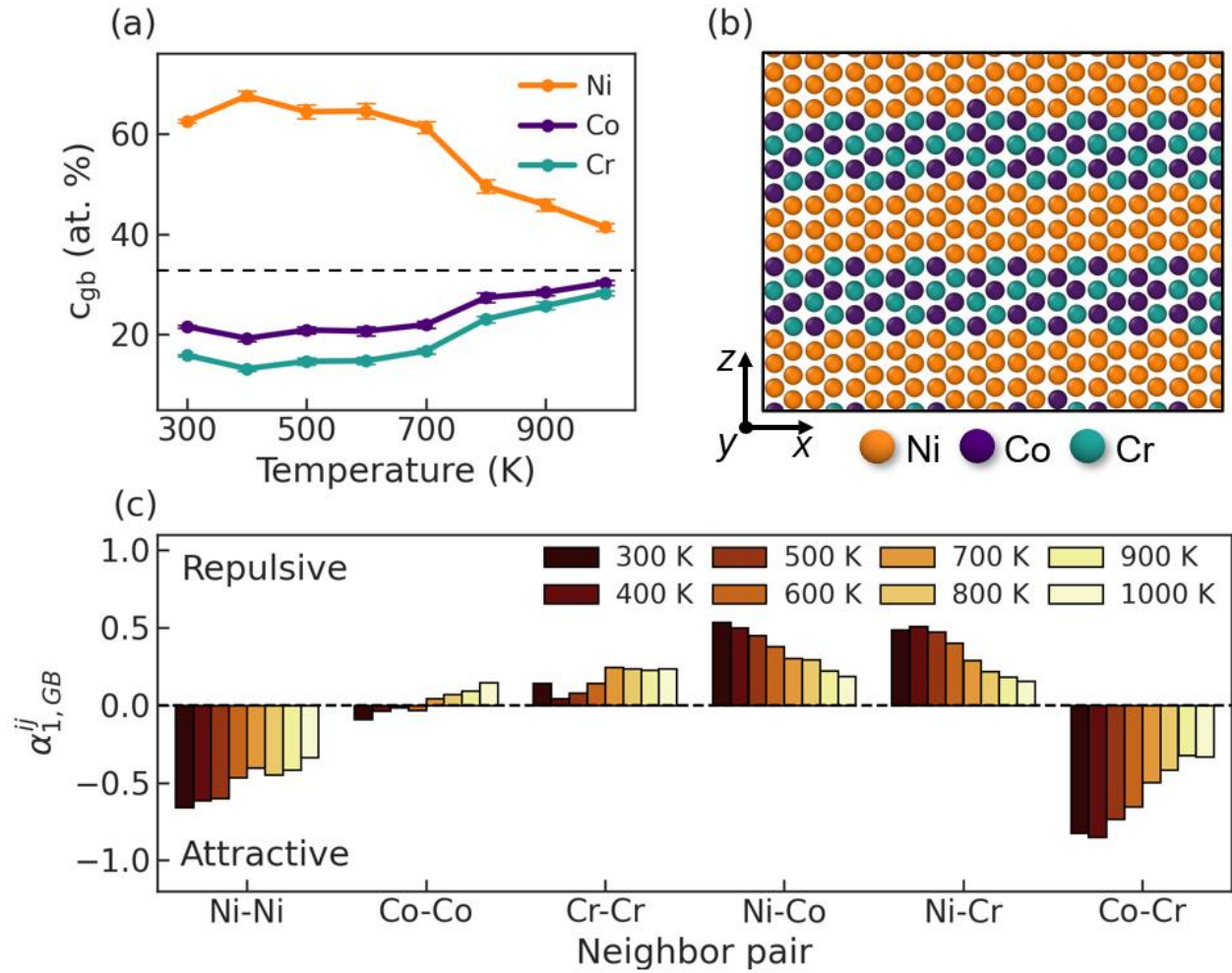


FIGURE 3. Grain boundary composition and chemical ordering behavior at temperatures from 300 to 1,000 K. (a) Grain boundary concentrations plotted as a function of temperature with the dashed line indicating equiatomic composition. (b) Elemental configurations in the grain boundary at 400 K, viewed looking into the grain boundary plane. (c) The grain boundary order parameter for pairwise species interactions plotted by temperature.

Figure 3(c) presents the grain boundary order parameter for each temperature and species pair. Ni-Ni and Co-Cr interactions dominate, as reflected by their large negative values compared to the mostly positive (repulsive) interactions of other pairs. Despite significant Ni segregation (Figure 3(a)), the magnitude of Ni-Ni interactions is smaller than that of Co-Cr, pointing to an anti-clustering effect for Ni and an enhanced chemical affinity for the latter pair due to co-segregation

and lower concentrations. For example, although Ni grain boundary enrichment exceeds 60 at. % at 400 K, $\alpha_{1,GB}^{Ni-Ni}$ is only -0.62 (~50% increase over bulk value), while $\alpha_{1,GB}^{Co-Cr}$ is -0.85 (~13% decrease over bulk value). Therefore, local Ni clustering at the grain boundary does not scale proportionally with its segregation level. These grain boundary results align with findings that higher global Ni concentrations in single-crystal models can reduce Ni clustering [73], confirming that grain boundary composition and interfacial ordering can also be influenced by global composition and related segregation behavior.

The comparable Ni clustering and Co-Cr ordering in both bulk and defect regions contrasts with the complex behavior seen in some other CCAs [13,74,75]. For example, in NbMoTaW, the strong Nb segregation to grain boundaries disrupts bulk ordering at the interface, despite significant Mo-Ta ordering within the grains [13]. Segregation can also be influenced by dynamic structural disorder induced by adsorption, which can either enhance or diminish segregation [74]. This variability in grain boundary behavior across CCAs underscores the broad range of grain boundary behaviors and equilibrium states, requiring further investigation to better understand the interplay of structure and chemistry in determining grain boundary properties.

B. Emergence of near-boundary compositional patterning

Previous studies have shown that segregation occurs not only at defects but also in regions adjacent to grain boundaries [13,32,66,76]. To fully capture segregation and ordering at interfaces in CCAs, it is crucial to analyze both the defect sites at the grain boundary and the nearby crystalline sites. To illustrate the compositional variation within the bicrystal after equilibration, concentrations were measured in atomic planes parallel to the grain boundary in the [113] direction. Figure 4(a) provides a spatial reference for plane indexing, while Figures 4(b)-(d)

present the elemental concentrations for each plane at 300 K. The highest Ni enrichment is observed at the central plane of each grain boundary, specifically at Planes 0 and 132 in Figure 4(b). Elemental fluctuations are also evident near the grain boundaries and, to a lesser extent, within the bulk regions. Notably, the pronounced Ni segregation does not lead to significant depletion of Ni within the grains, contrary to predictions by Wynblatt and Chatain [76] for polycrystals with grain sizes smaller than 100 nm. Figure 4(c) focuses on the grain boundary region centered at Plane 0 (red box in Figure 4(b)) to show the extended segregation profile in more detail. Within the grain boundary (Planes -1, 0, and 1), Ni is most enriched, while alternating Cr and Co peaks indicate their ordering tendency, even at the interface. Compositional oscillations extend into the bulk, forming periodic Ni-rich and Ni-depleted waves along the [113] axis, with antiphase fluctuations in Co and Cr. These waves originate at the interface and span ~60 atomic planes (about 6 nm). The most prominent Ni-depleted region adjacent to the grain boundary coincides with high Co and Cr concentrations (marked by black arrows in Figure 4(c)). Moving into the grain, Ni enrichment peaks above 50 at.%, with oscillations gradually diminishing away from the boundary.

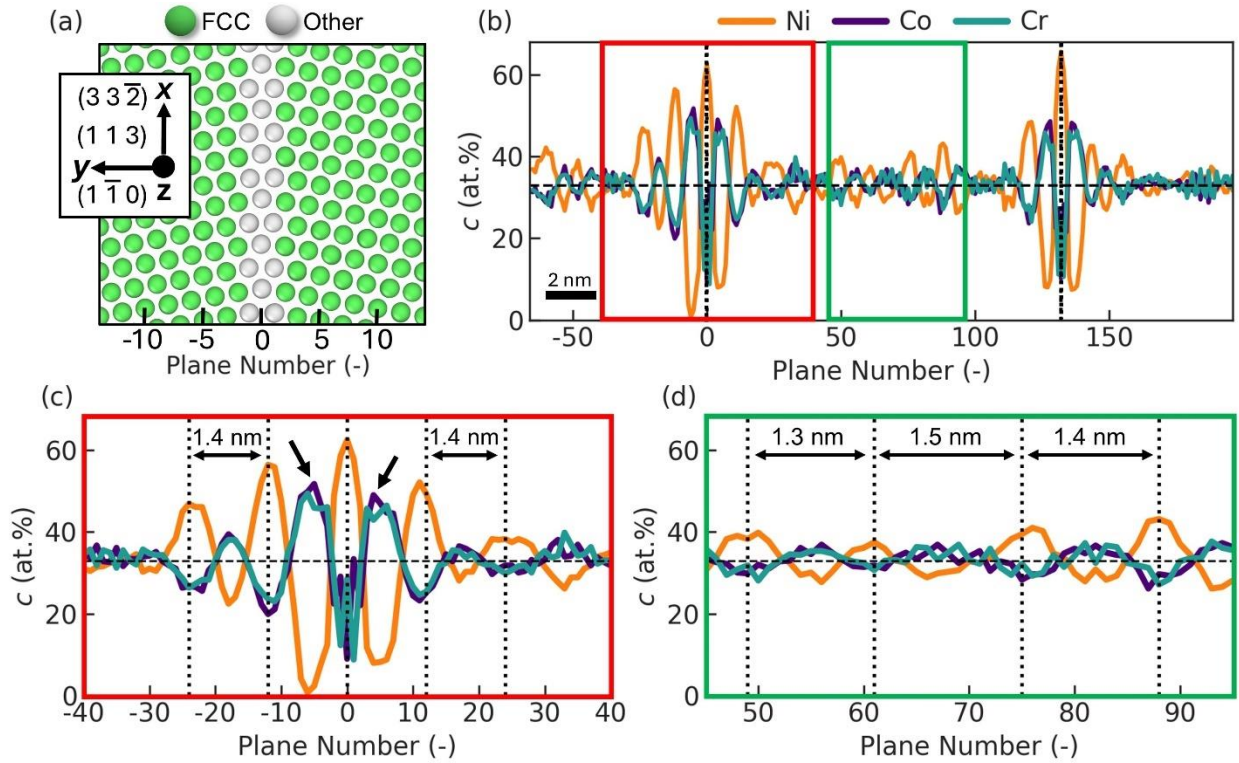


FIGURE 4. Grain boundary structure and its composition profiles at 300 K. (a) The $\Sigma 11$ grain boundary structure (white atoms) and FCC atoms (green). (b) Elemental concentrations, with dotted vertical lines highlighting the central grain boundary planes. Red and green boxes in (b) correspond to (c) grain boundary and (d) bulk regions for compositional analysis, respectively. The dotted vertical lines in (c) and (d) are centered on Ni peaks and show the ordering wavelength of ~ 1.4 nm. Arrows in (c) highlight the most prominent Ni-depletion region and corresponding Co-Cr enrichment.

Compositional waves were also observed in bulk regions, although of dramatically lower magnitude. Figure 4(d) shows compositional data from a bulk region (green box in Figure 4(b)), where compositional oscillations align along the $[113]$ axis even in the absence of a grain boundary. The dotted lines in Figure 4(d) highlight the Ni peaks, with the peak-to-peak distance representing the approximate ordering wavelength, spanning ~ 14 planes. Although Ni oscillations in the bulk only range from 27 to 40 at. % and are less pronounced in magnitude than those at the grain boundary, the ordering wavelength is similar to that near the grain boundary region. Both

regions demonstrate spatial ordering wavelengths of about 1.4 nm, which can be interpreted as the average ordered domain size when trying to compare with experimental studies [6,36].

The bulk compositional waves observed in Figure 4(d) suggest that experimental characterization techniques should be able to detect LCO in this system. However, typical TEM specimens are one to two orders of magnitude thicker than the bicrystal model used here, meaning that chemical ordered regions would be buried among larger volumes of material without the same order as one goes through the thickness. To explore this further, a thicker bicrystal model ($L_z = 20$ nm) was relaxed at 500 K, and planar compositions were again analyzed. Element concentrations as a function of plane are shown in Figures 5(a) and (b) for the thinner and thicker bicrystals, respectively. While compositional patterning is again observed at the grain boundaries (dotted vertical lines), the magnitude of fluctuations within the grains (black boxes) is significantly reduced in the thicker sample. This smoothing results from the overlap of Ni and Co-Cr clusters through the thickness of the larger sample, an effect that will be even more pronounced in a typical TEM specimen, with thicknesses usually being on the order of 50-100 nm.

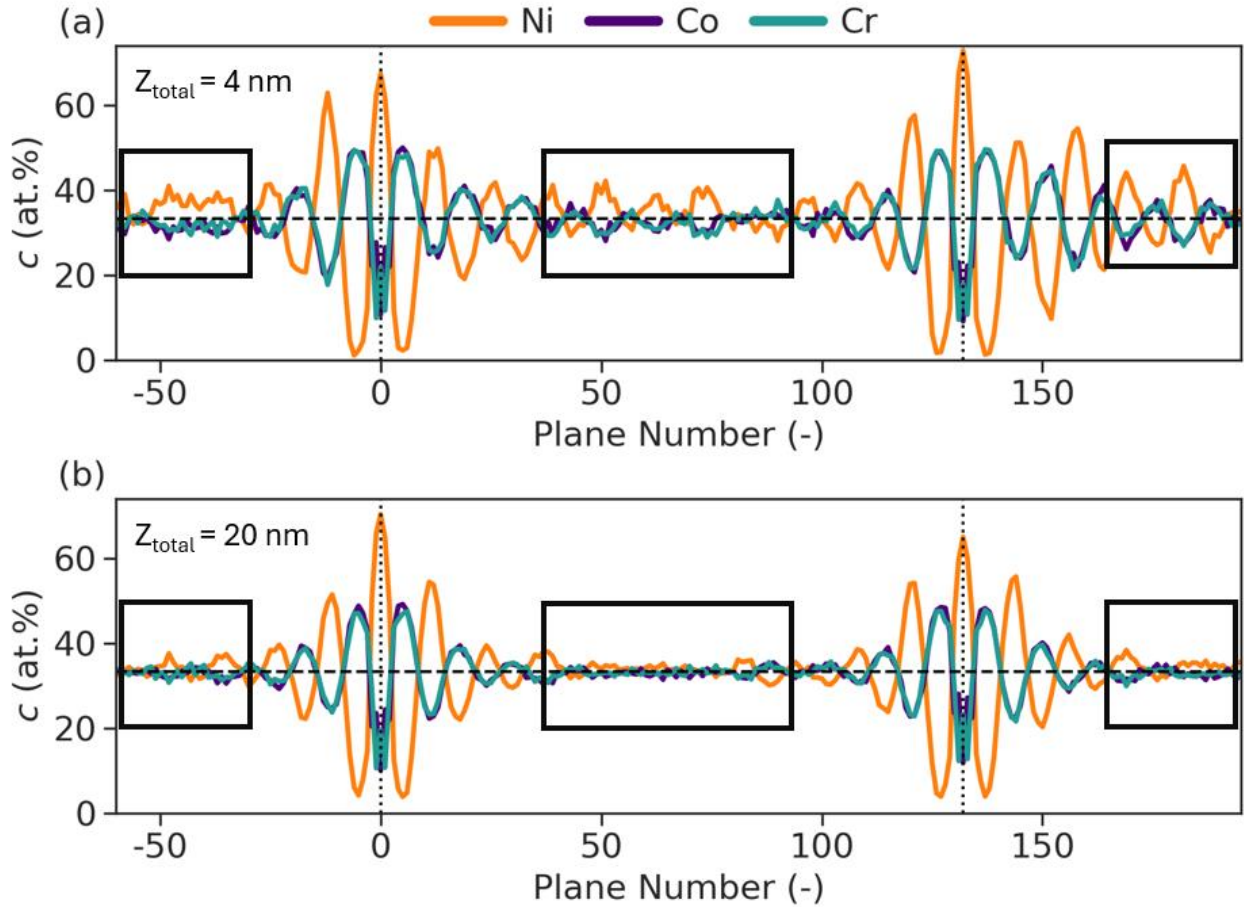


FIGURE 5. Local element compositions for samples with different thicknesses at 500 K. (a) Planar compositions for the thinner (4 nm) sample. (b) Planar compositions for the thicker (20 nm) sample. Black bounding boxes highlight bulk compositional fluctuations in the two samples.

To further illustrate the significance of the grain boundary patterning for experimental analysis of LCO, atomic snapshots were captured from both grain boundary and bulk regions at varying depths (z -direction) within the thicker sample, as shown in Figure 6(a). In each snapshot, the x and y coordinates remained constant while the depth increased by at least 2 nm, exceeding the characteristic ordering wavelength discussed earlier. Figures 6(b) and (c) compare atomic arrangements in the bulk and near the grain boundary, respectively. Grain boundary atoms in

Figure 6(c) are colored gray to draw attention to the adjacent crystalline sites. In the bulk (Figure 6(b)), Co-Cr ordering and Ni clustering shift positions as depth increases from Z_1 to Z_4 , constrained only by the formation of nearby clusters. For example, the green box highlights a region where a large Ni cluster at Z_1 is later replaced by Co and Cr atoms at Z_2 , with further variations observed at greater depth. This variation complicates LCO measurement, as electrons passing through such regions interact with diverse cluster configurations. In contrast, Figure 6(c) highlights the consistent Co and Cr occupation near the grain boundary throughout the sample thickness, where dashed green lines indicate a persistent Ni layer parallel to the grain boundary plane. This uniform structure creates a dense, ordered region which should allow for more accurate detection and quantification of LCO.

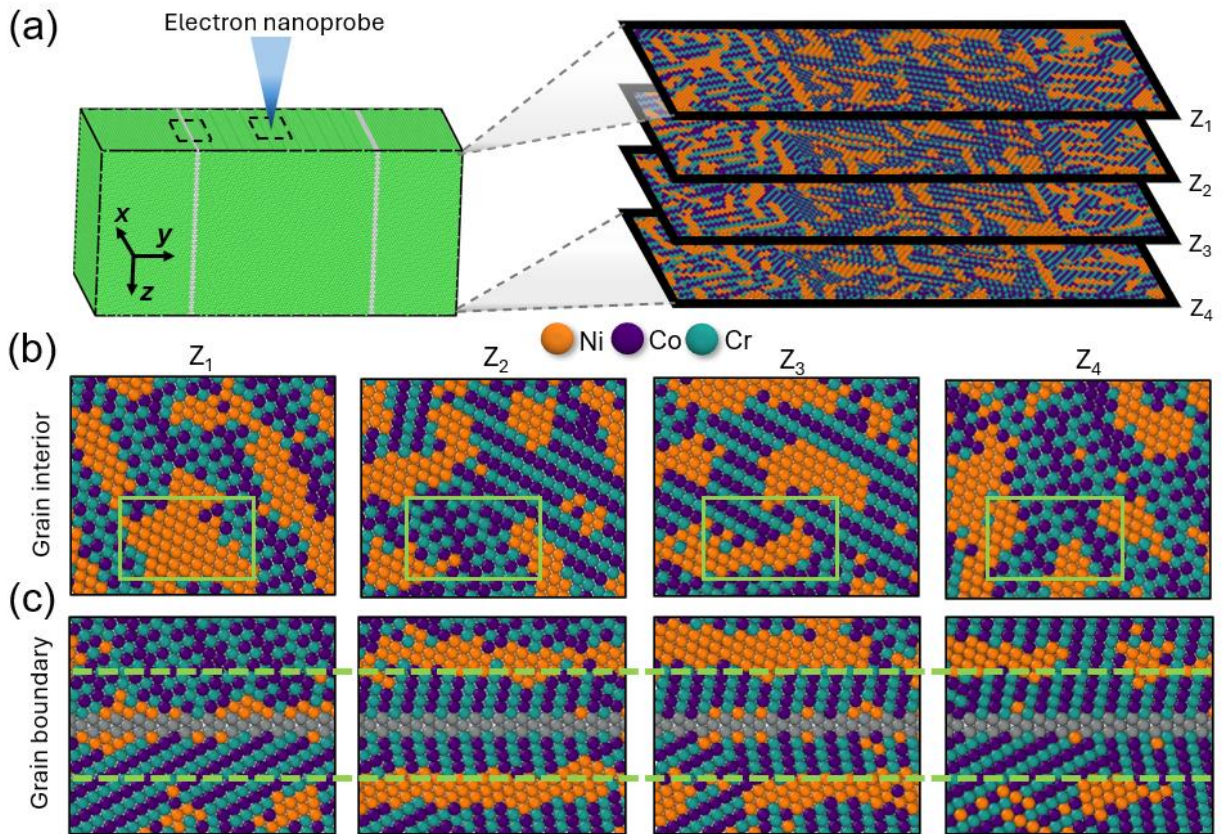


FIGURE 6. Spatial distributions of LCO throughout the sample. (a) Simulation cell of the thicker sample, colored by CNA, with dashed rectangles indicating approximate coordinates for atomic snapshots taken at varying depths (z -direction). (b) Atomic configurations from slices within bulk region, with depth increasing along Z_i . A green box in (b) highlights significant elemental fluctuation through the sample thickness. (c) Atomic configurations from slices near the grain boundary, with boundary atoms colored in gray to emphasize near-boundary composition. Green dashed lines in (c) denote the first layer of Ni enrichment near the boundary.

The advantages of investigating LCO near grain boundaries versus the bulk are schematically illustrated in Figure 7, where a hypothetical incident electron beam is aligned parallel to the grain boundary (x -direction in Figure 7(a)). At the interface, structural disorder and interfacial segregation act as a scaffold for localized saturation of LCO (Figure 7(b) and (c)). The application of an edge-on electron beam in this region is likely to produce signals rich in structural and chemical information about the LCO in the alloy. Furthermore, the LCO orientation is likely influenced by the grain boundary geometry, offering an additional microstructural lever for optimizing characterization. TEM-based techniques such as nanobeam diffraction or extended electron energy-loss fine structure analysis (EXELFS) [77], which employ nanometer-scale probe sizes to resolve local atomic structures, would be particularly well-suited for extracting chemical ordering information from these regions. In contrast, within the grain interior, electrons interact with tiny, isolated LCO pockets that may vary in orientation and/or can take on different morphologies depending on the selected zone axis (Figure 7(d) and (e)). Bulk regions sampled at random may therefore yield data that obscures the true LCO, complicating interpretation.

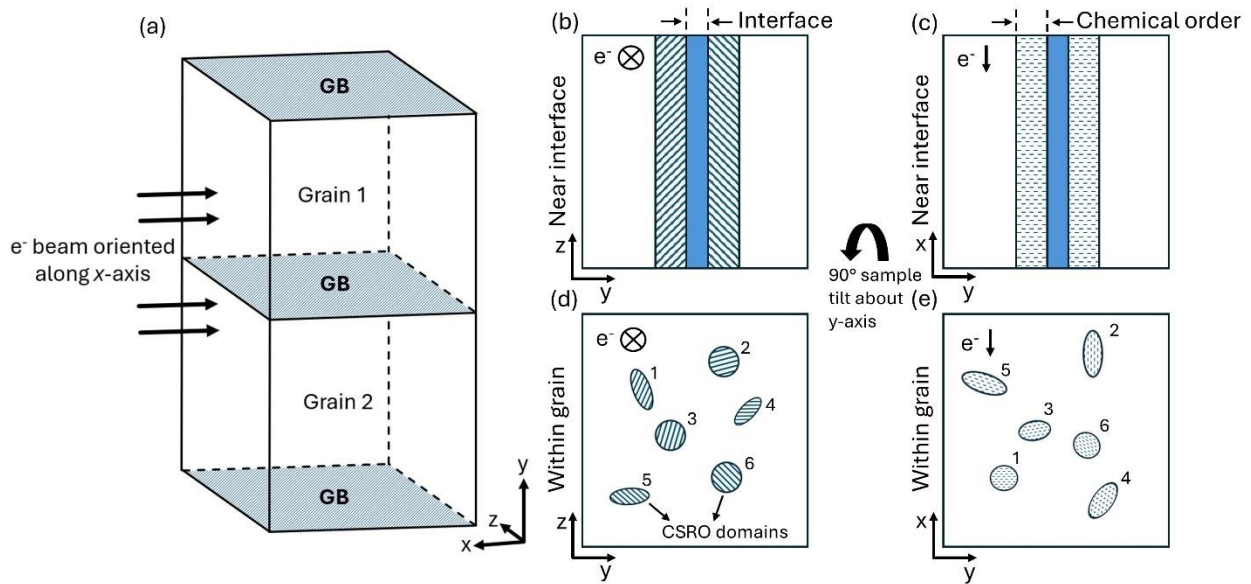


FIGURE 7. Schematic representation of electron beam interactions with LCO. (a) Orientation and electron beam direction with grain boundary regions abbreviated by GB. (b) y - z plane view of the interface and near-boundary compositional patterning, illustrating chemical order saturation along the grain boundary plane. (c) Rotation of the sample from (b) about the y -axis, showing the identical saturation of chemical order in the x - y plane. (d) y - z plane view of LCO within the grain interior, with circular and elliptical shapes depicting scattered regions of localized chemical order. (e) A 90° rotation of (d) around the y -axis. In (d) and (e), numbered LCO domains highlight variations in shape and position depending on the zone axis. In (b) and (d), the beam direction is into the page, while in (c) and (e) the beam is oriented top-down.

Figure 8 shows the segregation profiles across a temperature range of 300 K to 900 K, averaged over two grain boundaries per cell. Recall that the grain boundary spans planes -1 to 1 in each plot, where Ni enrichment is most pronounced. While the grain boundary segregation profile remains qualitatively consistent across all temperatures, its magnitude decreases notably at 900 K. Compositional patterning extends from the interface in each case, with increased attenuation observed at higher temperatures. For example, only a single Ni-enriched peak near the boundary is visible at 700 and 900 K (black arrows in Figures 8(c) and (d)), whereas multiple

peaks are observed at 300 K and 500 K (black arrows in Figures 8(a) and (b)). The broader compositionally-templated zone at 500 K compared to 300 K indicates stronger alignment with bulk chemical ordering perpendicular to the interface. This behavior reflects the energetic interplay between structure and chemistry. At 300 K, favorable bulk chemical ordering leads to larger clusters and isotropic domain growth within the grain. At 500 K (Figure 8(b)), a balance between anisotropic, structure-driven oscillations and bulk LCO formation results in a wider oscillation profile distance of approximately 7 nm.

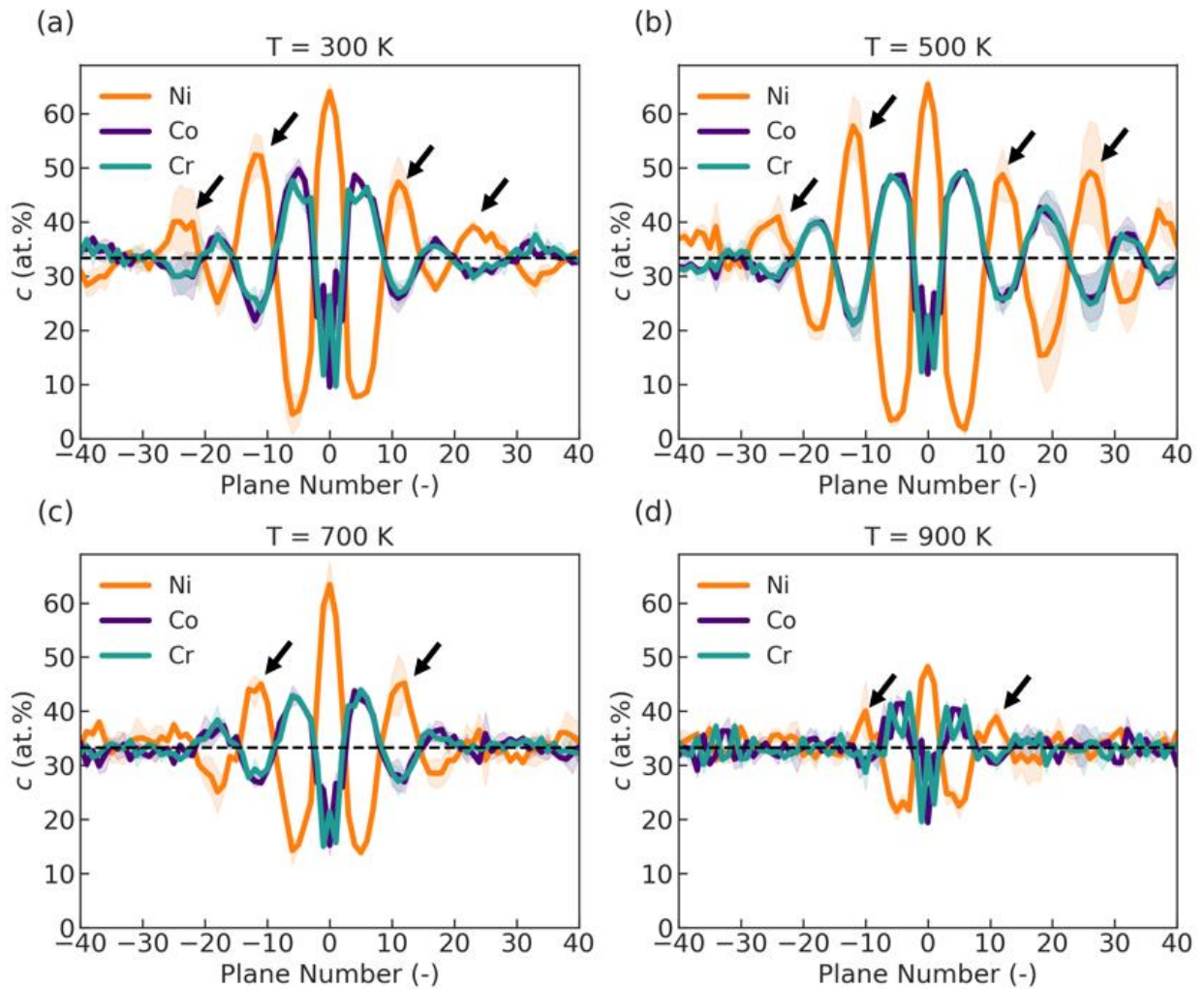


FIGURE 8. Near-boundary compositional patterning at temperatures of 300, 500, 700, and 900 K. Arrows in each plot highlight the Ni-enriched peaks that decline with increasing temperature.

As temperature increases, the level of LCO overall decreases due to the growing contribution of entropy to the Gibbs free energy. Besides the sparse distribution and small size of LCO clusters within grains, experimental detection is further complicated by chemical disorder induced by the high processing temperatures used for homogenization and heat treatment. Although nanobeam electron diffraction patterns have shown extra reflections related to LCO in CrCoNi after annealing at 873 K and 1273 K [5], much of the low-temperature bulk ordering is diminished by 900 K [15]. However, Co-Cr clustering near grain boundaries persists even at 900 K, indicating that chemical disordering is locally delayed in these regions due to solute segregation. This stabilization should enable the characterization of LCO under thermal conditions that facilitate sufficient atomic diffusion.

To investigate how the boundary structure and segregation state influence near-boundary patterns, the local structure at and near the interface was analyzed under two additional model conditions at 300 K: (1) a random solid solution condition and (2) a fully Ni-saturated condition. Figure 9 presents atomic models of these two boundaries along with their planar compositions and atomic volume profiles, with an MC/MD equilibrated boundary included for comparison. In the random solid solution, both the grain boundary and bulk are chemically disordered, while in the Ni-saturated boundary all defect sites are occupied by Ni atoms. Atomic volume was used to assess structural state as well as its correlation with segregation. In the random solid solution sample (Figure 9(a)), minor volumetric changes occur near the interface, with local atomic volumes decreasing by 0.35% for Ni and Co and 0.44% for Cr in Planes 3 and -3, compared to bulk averages (dashed lines in the third row of Figure 9(a)). These planes correspond to the first Co/Cr-enriched plane parallel to the interface in the equilibrated samples. Such structural

distortions are intrinsic to the interface structure and have also been predicted in pure metals [66]. In the Ni-saturated boundary, atomic volume decreases by 2.0%, 2.3%, and 2.8% for Ni, Co, and Cr, respectively, in Planes 3 and -3 (third row in Figure 9(b)). In CrCoNiFe-based CCAs, the near-boundary sites with maximum elastic compression (i.e. Planes 3/-3) serve as favorable segregation sites for smaller Fe atoms [66]. However, at the Ni-saturated boundary here (Figure 9(b)), the compressed region extends even further into the material away from the grain boundary defects. This extended compression arises from pronounced Ni segregation, which increases the grain boundary free volume and induces greater structural disorder in the adjacent crystalline sites.

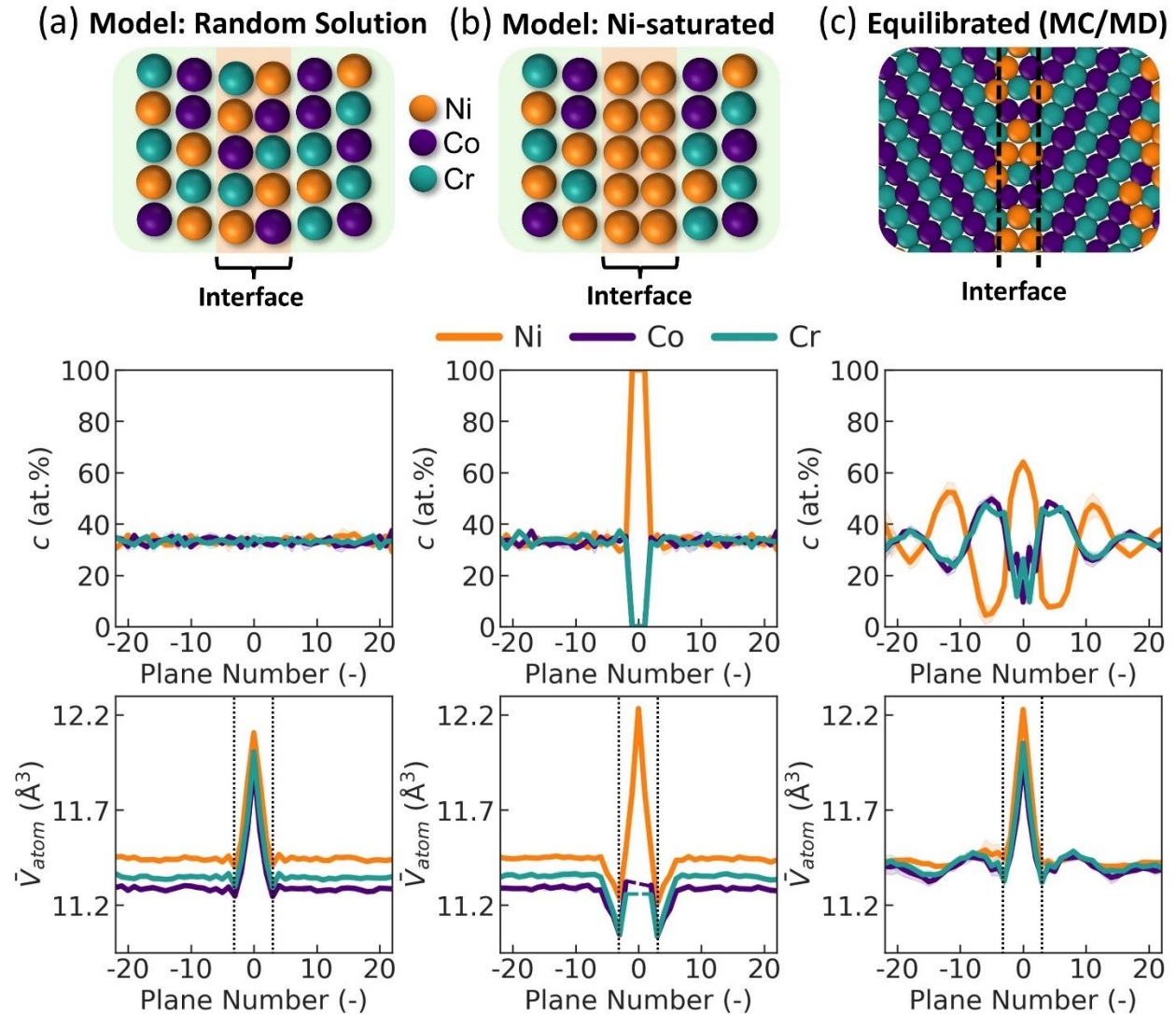


FIGURE 9. Structural and compositional variations for two limiting grain boundary conditions and their comparison with equilibrated boundary. Slices parallel to the grain boundary plane compare the random solid solution (a, first column), Ni-saturated boundary (b, second column), and an MC/MD equilibrated boundary (c, third column). Average atomic volumes for atoms within each plane and ordering condition are shown in the last row, where the dashed lines mark Planes 3 and -3, which exhibit the lowest atomic volume.

The effect of segregation on the equilibrated interface (Figure 9(c)) is more complex due to dynamic chemical and structural relaxation during the MC/MD process but displays key

characteristics observed in the model systems. Ni segregation induces volumetric compression in near-boundary planes, which subsequently attracts Co and Cr, mirroring the Co/Cr segregation observed at compressive regions of dislocations [78]. As this localized compression dissipates with increasing distance from the boundary, atomic volumes for all elements expand, creating conditions favorable for a secondary wave of Ni enrichment and giving rise to the near-boundary Ni peak. This structural oscillation drives the observed compositional pattern, which gradually fades as it propagates deeper into the grain.

Anisotropic compositional domain growth at defects, such as surface-directed spinodal decomposition (SDSD) [79], is a well-documented phenomenon. Jones et al. [80] first observed compositional waves with wave vectors normal to a surface in phase-separating poly(ethylenepropylene) and perdeuterated poly(ethylenepropylene) mixtures, which these authors attributed to the preferential wetting of the latter at the surface. Numerical simulations by Tang et al. [47] further elucidated the SDSD kinetic pathway in crystalline solids, showing that compositional patterning begins with segregation and preferential phase separation at the surface due to misfit stress relaxation, followed by isotropic domain growth within the bulk over time. Subsequent studies demonstrated that interfaces could also induce concentration waves propagating within a sample [46,49,81], creating compositional patterns closely resembling those described in Figures 4, 5 and 8. In CCAs, analogous mechanisms are likely active due to their diverse decomposition pathways that generate significant internal stress and are inevitably influenced by the presence of defects [53]. In CrCoNi, these stresses stem from multi-stage and sequential phase separations that locally alter the lattice constant due to compositional heterogeneities [50,53]. Additionally, enhanced diffusion kinetics near grain boundaries can produce depletion zones in certain alloys [82], potentially biasing the nucleation and growth of

chemically ordered structures in adjacent regions. This nanostructure patterning could be strategically exploited and controlled, emphasizing the importance of a more detailed investigation into the crystalline regions near boundaries in CCAs.

C. Validation of compositional patterning with a neural network potential

To ensure that the phenomenon described here is not an artifact of the chosen potential, a second set of limited simulations was performed using a new yet inefficient potential. One known limitation of the EAM potential used for the majority of this work is its inability to exactly match all pairwise chemical trends from DFT calculations. For example, while Tamm et al. [58] reported an attractive interaction between Cr and Ni using MC combined with *ab initio* energies, this EAM potential predicts a repulsive interaction between these elements. Such a discrepancy could be significant because the attractive Cr-Ni interaction is likely a critical component for accurately describing the dominant bonding preferences in the ternary alloy. Specifically, reduced Cr clustering driven by antiferromagnetic frustration from Cr-Cr nearest-neighbor interactions would promote greater Ni occupancy in Cr's coordination shell [26]. Consequently, a natural question is whether near-boundary behavior changes when such chemical interactions are accounted for. To address this, atomistic simulations of single-crystal and bicrystalline models were performed using a recently developed neural network potential (NNP) [60,61] designed to more accurately model LCO in CrCoNi. The NNP's flexible architecture allows it to represent the complex potential energy surface of a multicomponent alloy when trained on a high-quality DFT dataset. Unlike the EAM, the NNP captures attractive Cr-Ni and Cr-Co interactions, as well as Cr-Cr repulsion, in agreement with DFT-based MC simulations and experimental data [5,27,57,58]. Additionally, it reproduces superlattice chemical ordering patterns analogous to those experimentally observed by Zhou et al [5]. These patterns feature alternating Cr-enriched $\{113\}$ and $\{110\}$ planes interspersed

with Co and/or Ni-enriched planes. However, it is essential to note that the NNP also has practical limitations due to the increased complexity of its functional form for atomic interactions compared to the EAM potential. This added complexity reduces computational efficiency, necessitating significantly smaller simulation cell sizes when modeling the defect environment. Simply put, the wide variety of temperatures and segregation states reported on in the earlier parts of this manuscript would be intractable with this NNP in a reasonable amount of time.

Given the strong influence of chemical ordering on the near-boundary segregation in the EAM potential, an initial comparison of these parameters between the two potentials was performed. First, atom-swap based MC/MD simulations were conducted on a 4000-atom single-crystal cube relaxed at 200 K using the NNP with an MD timestep of 2.5 fs. Every 2 MD steps, one MC step was performed, with atom swaps attempted for 4% of the atoms. Figure 10(a) shows the Warren-Cowley parameter that describes bulk LCO tendencies for each nearest-neighbor chemical pair interaction for both the EAM potential and the NNP, where notable differences can be identified for the Ni-Ni, Ni-Cr, Co-Co, and Co-Cr interactions. For example, the strongly attractive Ni-Ni and Co-Cr interactions predicted by the EAM potential are reduced by more than half in the NNP, while the repulsive Ni-Cr and Co-Co interactions in the EAM are reversed to become attractive in the NNP. Importantly, the Ni-Cr interaction predicted by the NNP demonstrates better quantitative agreement with prior DFT studies [57,58].

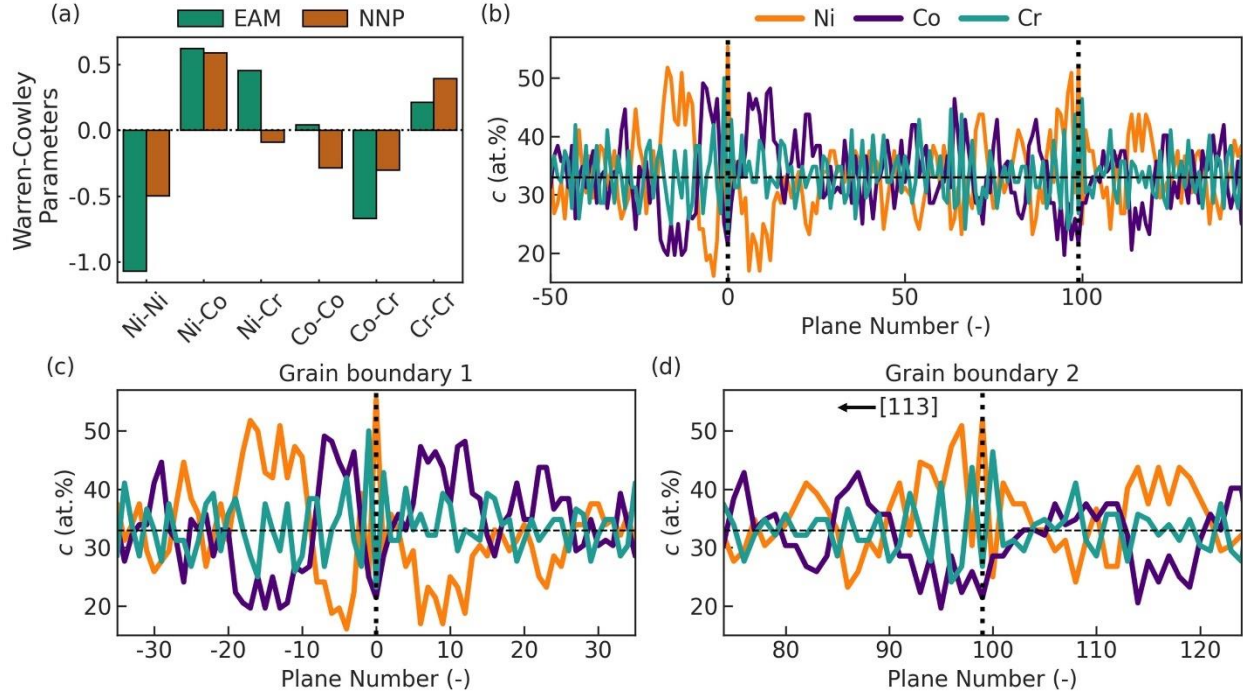


FIGURE 10. Chemical analysis of single-crystalline and bicrystalline models relaxed using the NNP. (a) Comparisons of the Warren-Cowley parameter between the EAM potential and the NNP. (b) Elemental concentrations for a sample at 200 K, with dotted vertical lines highlighting the central grain boundary planes. (c-d) Zoomed-in view spanning 6-7 nm at and near the left-hand and right-hand grain boundaries, respectively.

Next, MC/MD simulations were performed on bicrystalline models containing two symmetric $\Sigma 11$ grain boundaries at 200 K. To accommodate the extended simulation times required for full relaxation, the simulation cell dimensions were reduced to approximately $L_x \sim 3$ nm, $L_y \sim 21$ nm, and $L_z \sim 3$ nm, comprising only 22,176 atoms. The elongated y -dimension minimized grain boundary interactions and allowed chemical ordering to develop parallel to the interfaces. Figure 10(b) presents compositional profiles across $\{113\}$ planes parallel to the grain boundary after 1000 MC/MD steps. Dotted vertical lines in Figure 10(b) denote the positions of the two grain boundaries, with Ni enrichment localized at the central grain boundary plane and Cr enrichment at adjacent planes. The small cross-sectional area of the simulation cell introduced

compositional noise, manifesting as moderate elemental fluctuations throughout the sample between 25 and 41 at.%. Despite this, near-boundary compositional patterns are evident in Figures 10(c) and (d). In Figure 10(c), Ni depletion (~16 at.%) and Co enrichment (~49 at.%) occur on both sides of the boundary, similar to trends from simulations with the EAM potential. Notably, a wave-like pattern of alternating Ni and Co emerges on the left side of the boundary. At the second boundary (Figure 10(d)), the left side of the interface exhibits alternating Ni and Cr patterns consistent with the {113} plane ordering identified by Zhou et al. [5], with Cr peaks flanked by two layers of Ni enrichment. This pattern is amplified by the defect region but is asymmetric about the grain boundary plane. On the right side, Ni and Co waves are visible, though their clarity is reduced in part due to the compositional noise from the sample size. The concentration wave prominence may also depend on the symmetry across the boundary; when the symmetry is broken, the waves are less distinct and may have reduced magnitudes.

Additional MC/MD steps (6000 total) show further reduction of potential energy (Figure S1). While the grain boundary patterns remain largely unchanged at later steps (Figure S2), bulk ordering oscillations become more pronounced, reducing the prominence of near-boundary patterns. Larger simulation cells are expected to reduce these bulk oscillations while preserving the interfaces as anchor points for preferential ordering alignment, as observed with the EAM potential in Figure 5. On balance, the chemical patterns predicted by the EAM potential are largely reproduced by the NNP, with some expected deviations due to differences in the chemical ordering behavior and inherent simulation size/time limitations. Despite these minor discrepancies, the consistent grain boundary-localized compositional patterning highlights the potential for predictable isolation and analysis.

The compositional patterning and localized chemical ordering observed near grain boundaries likely have significant implications for grain boundary mobility and microstructural evolution in CCAs at high temperatures. As grain boundaries migrate, they must overcome both the energetic barriers associated with structure shuffling at the interface and the additional resistance created by the ordered compositional waves extending into the grain. This chemical drag effect would be particularly pronounced at lower temperatures where the compositional patterns are more stable and extend further into the grain interior. The migration of these interfaces would require disrupting this extended ordered zone, potentially leading to sluggish grain growth kinetics. This mechanism differs from traditional solute drag, where individual segregated atoms create localized energetic barriers. Instead, the collective rearrangement of ordered domains during boundary motion could create a more substantial kinetic barrier, especially considering the strong Co-Cr ordering observed adjacent to the interface. Such ordering-induced drag effects could contribute to the exceptional thermal stability reported in some CCAs [22–24].

It is important to note that while this study focuses on a single boundary geometry within a specific alloy class, the underlying physical principles are broadly applicable and likely relevant to other CCAs and grain boundary configurations. Based on the present work and recent studies [13,66], we hypothesize that chemical transitions near interfaces are a common, if not ubiquitous, feature in CCAs with strong chemical ordering tendencies and some degree of grain boundary segregation. Moreover, strategic selection of grain boundary geometry could enable tailored compositional patterns. For example, coherent twin boundaries with minimal segregation and structural disorder may remain chemically homogeneous, as demonstrated by Li et al. [18]. In contrast, high-angle boundaries with strong segregation and aligned along preferential ordering planes may significantly amplify compositional patterns. Investigating mixed boundaries provides

an efficient pathway for sampling various ordering vectors, potentially resulting in long-range, anisotropic compositional patterns such as those observed in cermets [83] and a Pt-3 at.% Ni alloy [84].

IV. SUMMARY AND CONCLUSIONS

In this study, simulations and analysis of compositional patterning and LCO at a $\Sigma 11$ $\langle 110 \rangle$ symmetric tilt boundary in equiatomic CrCoNi lead to the following conclusions:

- 1) Ni enrichment drives segregation behavior at low and intermediate temperatures, while Co and Cr exhibit co-segregation, as evidenced by their similar depletion rates. Despite pronounced Ni segregation, a grain boundary chemical order parameter reveals enhanced Co-Cr ordering at the interface that is accompanied by reduction in Ni-Ni clustering.
- 2) Concentration waves characterized by periodic enrichment and depletion of Ni with antiphase oscillations in Co and Cr propagate from the grain boundary with a wave vector normal to the grain boundary plane. Ni depletion zones adjacent to defect sites promote the symmetric ordering of Co and Cr in the vicinity of the interface. Weaker, yet similar, oscillations observed deeper in the grain suggest a shared underlying ordering mechanism, as indicated by their comparable wavelength.
- 3) Simulations of thicker bicrystal models demonstrate uniform Co-Cr enrichment along the grain boundary throughout the sample's thickness. However, comparisons at various depths within the grain show that transient chemical domains can fluctuate without the grain boundary as a structural template. This would complicate TEM analysis of thicker samples, while the chemical ordering near the interface should enhance the detectability of LCO with these methods.

- 4) The formation of the compositional nanopatterning occurs at all temperatures, but both the magnitude and width of oscillations are temperature-dependent. At higher temperatures, only a single Ni-depletion peak emerges, likely due to structural effects from interfacial relaxation, as supported by additional models.
- 5) Atomistic simulations using a NNP developed for CrCoNi emphasize that variability in chemical ordering behavior is dependent on the choice of interatomic potential yet confirm that grain boundary segregation can amplify and localize chemical ordered in the near-boundary region.

Overall, the results of this study highlight the coupling of grain boundary segregation and chemical ordering patterns. These findings suggest that future experimental characterization of LCO should focus on the compositional variations induced by segregation and structural relaxation at and near defects. Furthermore, the concept of long-range, structurally-templated compositional manipulation marks a significant step forward in microstructural design, offering a powerful tool for engineering microstructural features and therefore material properties within the complex CCA landscape.

ACKNOWLEDGMENTS

This paper was supported by the National Science Foundation Materials Research Science and Engineering Center program through the UC Irvine Center for Complex and Active Materials (DMR-2011967).

REFERENCES

- [1] S. Gorsse, J.-P. Couzinié, D.B. Miracle, From high-entropy alloys to complex concentrated alloys, *Comptes Rendus Physique* 19 (2018) 721–736. <https://doi.org/10.1016/j.crhy.2018.09.004>.
- [2] X. Wu, Chemical short-range orders in high-/medium-entropy alloys, *Journal of Materials Science & Technology* 147 (2023) 189–196. <https://doi.org/10.1016/j.jmst.2022.10.070>.
- [3] W. Chen, L. Li, Q. Zhu, H. Zhuang, Chemical short-range order in complex concentrated alloys, *MRS Bulletin* 48 (2023) 762–768. <https://doi.org/10.1557/s43577-023-00575-8>.
- [4] X. Chen, Q. Wang, Z. Cheng, M. Zhu, H. Zhou, P. Jiang, L. Zhou, Q. Xue, F. Yuan, J. Zhu, X. Wu, E. Ma, Direct observation of chemical short-range order in a medium-entropy alloy, *Nature* 592 (2021) 712–716. <https://doi.org/10.1038/s41586-021-03428-z>.
- [5] L. Zhou, Q. Wang, J. Wang, X. Chen, P. Jiang, H. Zhou, F. Yuan, X. Wu, Z. Cheng, E. Ma, Atomic-scale evidence of chemical short-range order in CrCoNi medium-entropy alloy, *Acta Materialia* 224 (2022) 117490. <https://doi.org/10.1016/j.actamat.2021.117490>.
- [6] J. Wang, P. Jiang, F. Yuan, X. Wu, Chemical medium-range order in a medium-entropy alloy, *Nat Commun* 13 (2022) 1021. <https://doi.org/10.1038/s41467-022-28687-w>.
- [7] S. Zhao, Role of chemical disorder and local ordering on defect evolution in high-entropy alloys, *Phys. Rev. Mater.* 5 (2021) 103604. <https://doi.org/10.1103/PhysRevMaterials.5.103604>.
- [8] P. Cao, How Does Short-Range Order Impact Defect Kinetics in Irradiated Multiprincipal Element Alloys?, *Acc. Mater. Res.* 2 (2021) 71–74. <https://doi.org/10.1021/accountsmr.0c00102>.
- [9] B. Xing, W. Zou, T.J. Rupert, P. Cao, Vacancy diffusion barrier spectrum and diffusion correlation in multicomponent alloys, *Acta Materialia* 266 (2024) 119653. <https://doi.org/10.1016/j.actamat.2024.119653>.
- [10] S. Yin, J. Ding, M. Asta, R.O. Ritchie, Ab initio modeling of the energy landscape for screw dislocations in body-centered cubic high-entropy alloys, *Npj Comput Mater* 6 (2020) 1–11. <https://doi.org/10.1038/s41524-020-00377-5>.
- [11] H. Zheng, L.T.W. Fey, X.-G. Li, Y.-J. Hu, L. Qi, C. Chen, S. Xu, I.J. Beyerlein, S.P. Ong, Multi-scale investigation of short-range order and dislocation glide in MoNbTi and TaNbTi multi-principal element alloys, *Npj Comput Mater* 9 (2023) 1–13. <https://doi.org/10.1038/s41524-023-01046-z>.
- [12] X.-T. Li, X.-Z. Tang, Y.-F. Guo, Inhibition effect of segregation and chemical order on grain boundary migration in NbMoTaW multi-principal element alloy, *Scripta Materialia* 235 (2023) 115632. <https://doi.org/10.1016/j.scriptamat.2023.115632>.
- [13] D. Aksoy, M.J. McCarthy, I. Geiger, D. Apelian, H. Hahn, E.J. Lavernia, J. Luo, H. Xin, T.J. Rupert, Chemical order transitions within extended interfacial segregation zones in NbMoTaW, *Journal of Applied Physics* 132 (2022) 235302. <https://doi.org/10.1063/5.0122502>.

- [14] F. Cao, Y. Chen, S. Zhao, E. Ma, L. Dai, Grain boundary phase transformation in a CrCoNi complex concentrated alloy, *Acta Materialia* 209 (2021) 116786. <https://doi.org/10.1016/j.actamat.2021.116786>.
- [15] Q.-J. Li, H. Sheng, E. Ma, Strengthening in multi-principal element alloys with local-chemical-order roughened dislocation pathways, *Nat Commun* 10 (2019) 3563. <https://doi.org/10.1038/s41467-019-11464-7>.
- [16] R. Pasianot, D. Farkas, Atomistic modeling of dislocations in a random quinary high-entropy alloy, *Computational Materials Science* 173 (2020) 109366. <https://doi.org/10.1016/j.commatsci.2019.109366>.
- [17] S. Lee, M.J. Duarte, M. Feuerbacher, R. Soler, C. Kirchlechner, C.H. Liebscher, S.H. Oh, G. Dehm, Dislocation plasticity in FeCoCrMnNi high-entropy alloy: quantitative insights from in situ transmission electron microscopy deformation, *Materials Research Letters* 8 (2020) 216–224. <https://doi.org/10.1080/21663831.2020.1741469>.
- [18] L. Li, R.D. Kamachali, Z. Li, Z. Zhang, Grain boundary energy effect on grain boundary segregation in an equiatomic high-entropy alloy, *Phys. Rev. Materials* 4 (2020) 053603. <https://doi.org/10.1103/PhysRevMaterials.4.053603>.
- [19] L. Li, Z. Li, A. Kwiatkowski da Silva, Z. Peng, H. Zhao, B. Gault, D. Raabe, Segregation-driven grain boundary spinodal decomposition as a pathway for phase nucleation in a high-entropy alloy, *Acta Materialia* 178 (2019) 1–9. <https://doi.org/10.1016/j.actamat.2019.07.052>.
- [20] I. Geiger, D. Apelian, X. Pan, P. Cao, J. Luo, T.J. Rupert, Frustrated metastable-to-equilibrium grain boundary structural transition in NbMoTaW due to segregation and chemical complexity, *Acta Materialia* 272 (2024) 119939. <https://doi.org/10.1016/j.actamat.2024.119939>.
- [21] C. Baruffi, W.A. Curtin, Theory of spontaneous grain boundary roughening in high entropy alloys, *Acta Materialia* 234 (2022) 118011. <https://doi.org/10.1016/j.actamat.2022.118011>.
- [22] W.H. Liu, Y. Wu, J.Y. He, T.G. Nieh, Z.P. Lu, Grain growth and the Hall–Petch relationship in a high-entropy FeCrNiCoMn alloy, *Scripta Materialia* 68 (2013) 526–529. <https://doi.org/10.1016/j.scriptamat.2012.12.002>.
- [23] Z. Wu, H. Bei, F. Otto, G.M. Pharr, E.P. George, Recovery, recrystallization, grain growth and phase stability of a family of FCC-structured multi-component equiatomic solid solution alloys, *Intermetallics* 46 (2014) 131–140. <https://doi.org/10.1016/j.intermet.2013.10.024>.
- [24] D. Utt, A. Stukowski, K. Albe, Grain boundary structure and mobility in high-entropy alloys: A comparative molecular dynamics study on a $\Sigma 11$ symmetrical tilt grain boundary in face-centered cubic CuNiCoFe, *Acta Materialia* 186 (2020) 11–19. <https://doi.org/10.1016/j.actamat.2019.12.031>.
- [25] P. Sathiyamoorthi, J. Basu, S. Kashyap, K.G. Pradeep, R.S. Kottada, Thermal stability and grain boundary strengthening in ultrafine-grained CoCrFeNi high entropy alloy composite, *Materials & Design* 134 (2017) 426–433. <https://doi.org/10.1016/j.matdes.2017.08.053>.

- [26] F. Walsh, M. Asta, R.O. Ritchie, Magnetically driven short-range order can explain anomalous measurements in CrCoNi, *Proc. Natl. Acad. Sci. U.S.A.* 118 (2021) e2020540118. <https://doi.org/10.1073/pnas.2020540118>.
- [27] F.X. Zhang, S. Zhao, K. Jin, H. Xue, G. Velisa, H. Bei, R. Huang, J.Y.P. Ko, D.C. Pagan, J.C. Neufeind, W.J. Weber, Y. Zhang, Local Structure and Short-Range Order in a NiCoCr Solid Solution Alloy, *Phys. Rev. Lett.* 118 (2017) 205501. <https://doi.org/10.1103/PhysRevLett.118.205501>.
- [28] W.-R. Jian, Z. Xie, S. Xu, Y. Su, X. Yao, I.J. Beyerlein, Effects of lattice distortion and chemical short-range order on the mechanisms of deformation in medium entropy alloy CoCrNi, *Acta Materialia* 199 (2020) 352–369. <https://doi.org/10.1016/j.actamat.2020.08.044>.
- [29] S. Chen, Z.H. Aitken, S. Pattamatta, Z. Wu, Z.G. Yu, D.J. Srolovitz, P.K. Liaw, Y.-W. Zhang, Simultaneously enhancing the ultimate strength and ductility of high-entropy alloys via short-range ordering, *Nat Commun* 12 (2021) 4953. <https://doi.org/10.1038/s41467-021-25264-5>.
- [30] E. Antillon, C. Woodward, S.I. Rao, B. Akdim, T.A. Parthasarathy, Chemical short range order strengthening in a model FCC high entropy alloy, *Acta Materialia* 190 (2020) 29–42. <https://doi.org/10.1016/j.actamat.2020.02.041>.
- [31] S. Yin, Y. Zuo, A. Abu-Odeh, H. Zheng, X.-G. Li, J. Ding, S.P. Ong, M. Asta, R.O. Ritchie, Atomistic simulations of dislocation mobility in refractory high-entropy alloys and the effect of chemical short-range order, *Nat Commun* 12 (2021) 4873. <https://doi.org/10.1038/s41467-021-25134-0>.
- [32] X.-G. Li, C. Chen, H. Zheng, Y. Zuo, S.P. Ong, Complex strengthening mechanisms in the NbMoTaW multi-principal element alloy, *Npj Comput Mater* 6 (2020) 70. <https://doi.org/10.1038/s41524-020-0339-0>.
- [33] X. Huang, L. Liu, X. Duan, W. Liao, J. Huang, H. Sun, C. Yu, Atomistic simulation of chemical short-range order in HfNbTaZr high entropy alloy based on a newly-developed interatomic potential, *Materials & Design* 202 (2021) 109560. <https://doi.org/10.1016/j.matdes.2021.109560>.
- [34] I. Geiger, J. Luo, E.J. Lavernia, P. Cao, D. Apelian, T.J. Rupert, Influence of chemistry and structure on interfacial segregation in NbMoTaW with high-throughput atomistic simulations, *Journal of Applied Physics* 132 (2022) 235301. <https://doi.org/10.1063/5.0130402>.
- [35] G. Van Tendeloo, S. Amelinckx, The origin of diffuse intensity in electron diffraction patterns, *Phase Transitions* 67 (1998) 101–135. <https://doi.org/10.1080/01411599808219190>.
- [36] R. Zhang, S. Zhao, J. Ding, Y. Chong, T. Jia, C. Ophus, M. Asta, R.O. Ritchie, A.M. Minor, Short-range order and its impact on the CrCoNi medium-entropy alloy, *Nature* 581 (2020) 283–287. <https://doi.org/10.1038/s41586-020-2275-z>.
- [37] R. Zhang, S. Zhao, C. Ophus, Y. Deng, S.J. Vachhani, B. Ozdol, R. Traylor, K.C. Bustillo, J.W. Morris, D.C. Chrzan, M. Asta, A.M. Minor, Direct imaging of short-range order and its

impact on deformation in Ti-6Al, *Science Advances* 5 (n.d.) eaax2799. <https://doi.org/10.1126/sciadv.aax2799>.

[38] D. Liu, Q. Wang, J. Wang, X.F. Chen, P. Jiang, F.P. Yuan, Z.Y. Cheng, E. Ma, X.L. Wu, Chemical short-range order in Fe₅₀Mn₃₀Co₁₀Cr₁₀ high-entropy alloy, *Materials Today Nano* 16 (2021) 100139. <https://doi.org/10.1016/j.mtnano.2021.100139>.

[39] Z.G. Wang, W. Zhou, L.M. Fu, J.F. Wang, R.C. Luo, X.C. Han, B. Chen, X.D. Wang, Effect of coherent L12 nanoprecipitates on the tensile behavior of a fcc-based high-entropy alloy, *Materials Science and Engineering: A* 696 (2017) 503–510. <https://doi.org/10.1016/j.msea.2017.04.111>.

[40] X. Chen, F. Yuan, H. Zhou, X. Wu, Structure motif of chemical short-range order in a medium-entropy alloy, *Materials Research Letters* 10 (2022) 149–155. <https://doi.org/10.1080/21663831.2022.2029607>.

[41] F. Walsh, M. Zhang, R.O. Ritchie, A.M. Minor, M. Asta, Extra electron reflections in concentrated alloys do not necessitate short-range order, *Nat. Mater.* 22 (2023) 926–929. <https://doi.org/10.1038/s41563-023-01570-9>.

[42] F. Walsh, M. Zhang, R.O. Ritchie, M. Asta, A.M. Minor, Multiple origins of extra electron diffractions in fcc metals, *Science Advances* 10 (2024) eadn9673. <https://doi.org/10.1126/sciadv.adn9673>.

[43] F.G. Coury, C. Miller, R. Field, M. Kaufman, On the origin of diffuse intensities in fcc electron diffraction patterns, *Nature* 622 (2023) 742–747. <https://doi.org/10.1038/s41586-023-06530-6>.

[44] L. Li, Z. Chen, S. Kuroiwa, M. Ito, K. Yuge, K. Kishida, H. Tanimoto, Y. Yu, H. Inui, E.P. George, Evolution of short-range order and its effects on the plastic deformation behavior of single crystals of the equiatomic Cr-Co-Ni medium-entropy alloy, *Acta Materialia* 243 (2023) 118537. <https://doi.org/10.1016/j.actamat.2022.118537>.

[45] J.B. Seol, W.-S. Ko, S.S. Sohn, M.Y. Na, H.J. Chang, Y.-U. Heo, J.G. Kim, H. Sung, Z. Li, E. Pereloma, H.S. Kim, Mechanically derived short-range order and its impact on the multi-principal-element alloys, *Nat Commun* 13 (2022) 6766. <https://doi.org/10.1038/s41467-022-34470-8>.

[46] H. Ramanarayan, T.A. Abinandanan, Phase field study of grain boundary effects on spinodal decomposition, *Acta Materialia* 51 (2003) 4761–4772. [https://doi.org/10.1016/S1359-6454\(03\)00301-X](https://doi.org/10.1016/S1359-6454(03)00301-X).

[47] M. Tang, A. Karma, Surface Modes of Coherent Spinodal Decomposition, *Phys. Rev. Lett.* 108 (2012) 265701. <https://doi.org/10.1103/PhysRevLett.108.265701>.

[48] Y.-S. Li, S.-X. Li, T.-Y. Zhang, Effect of dislocations on spinodal decomposition in Fe–Cr alloys, *Journal of Nuclear Materials* 395 (2009) 120–130. <https://doi.org/10.1016/j.jnucmat.2009.10.042>.

- [49] Y.-Y. Deng, C. Guo, J.-C. Wang, Q. Liu, Y.-P. Zhao, Q. Yang, Phase-field study of spinodal decomposition under effect of grain boundary*, *Chinese Phys. B* 30 (2021) 088101. <https://doi.org/10.1088/1674-1056/abea9b>.
- [50] D.L. Foley, A.K. Barnett, Y. Rakita, A. Perez, P.P. Das, S. Nicolopoulos, D.E. Spearot, I.J. Beyerlein, M.L. Falk, M.L. Taheri, Diffuse electron scattering reveals kinetic frustration as origin of order in CoCrNi medium entropy alloy, *Acta Materialia* 268 (2024) 119753. <https://doi.org/10.1016/j.actamat.2024.119753>.
- [51] Y. Wang, M. Jiao, Y. Wu, X. Liu, H. Wang, S. Jiang, X. Zhang, Z. Lu, Enhancing properties of high-entropy alloys via manipulation of local chemical ordering, *Journal of Materials Science & Technology* 180 (2024) 23–31. <https://doi.org/10.1016/j.jmst.2023.10.003>.
- [52] A. Jagetia, M.S.K.K.Y. Nartu, S. Dasari, A. Sharma, B. Gwalani, R. Banerjee, Ordering-mediated local nano-clustering results in unusually large Hall-Petch strengthening coefficients in high entropy alloys, *Materials Research Letters* 9 (2021) 213–222. <https://doi.org/10.1080/21663831.2020.1871440>.
- [53] P.-Y. Cao, F. Liu, F.-P. Yuan, E. Ma, X.-L. Wu, Multiple potential phase-separation paths in multi-principal element alloys, *Materials Today Nano* 28 (2024) 100511. <https://doi.org/10.1016/j.mtnano.2024.100511>.
- [54] H.-W. Hsiao, R. Feng, H. Ni, K. An, J.D. Poplawsky, P.K. Liaw, J.-M. Zuo, Data-driven electron-diffraction approach reveals local short-range ordering in CrCoNi with ordering effects, *Nat Commun* 13 (2022) 6651. <https://doi.org/10.1038/s41467-022-34335-0>.
- [55] Y. Han, H. Chen, Y. Sun, J. Liu, S. Wei, B. Xie, Z. Zhang, Y. Zhu, M. Li, J. Yang, W. Chen, P. Cao, Y. Yang, Ubiquitous short-range order in multi-principal element alloys, *Nat Commun* 15 (2024) 6486. <https://doi.org/10.1038/s41467-024-49606-1>.
- [56] F. Cao, Y. Chen, H.-Y. Wang, L.-H. Dai, Chemical inhomogeneity inhibits grain boundary fracture: A comparative study in CrCoNi medium entropy alloy, *Journal of Materials Science & Technology* 153 (2023) 228–241. <https://doi.org/10.1016/j.jmst.2023.02.002>.
- [57] J. Ding, Q. Yu, M. Asta, R.O. Ritchie, Tunable stacking fault energies by tailoring local chemical order in CrCoNi medium-entropy alloys, *Proceedings of the National Academy of Sciences* 115 (2018) 8919–8924. <https://doi.org/10.1073/pnas.1808660115>.
- [58] A. Tamm, A. Aabloo, M. Klintonberg, M. Stocks, A. Caro, Atomic-scale properties of Ni-based FCC ternary, and quaternary alloys, *Acta Materialia* 99 (2015) 307–312. <https://doi.org/10.1016/j.actamat.2015.08.015>.
- [59] M. Mizuno, H. Araki, Structural evolution of short-range order in CrCoNi and MnCoNi medium-entropy alloys, *Phys. Rev. Mater.* 8 (2024) 013601. <https://doi.org/10.1103/PhysRevMaterials.8.013601>.

- [60] A. Singraber, J. Behler, C. Dellago, Library-Based LAMMPS Implementation of High-Dimensional Neural Network Potentials, *J. Chem. Theory Comput.* 15 (2019) 1827–1840. <https://doi.org/10.1021/acs.jctc.8b00770>.
- [61] J.-P. Du, P. Yu, S. Shinzato, F.-S. Meng, Y. Sato, Y. Li, Y. Fan, S. Ogata, Chemical domain structure and its formation kinetics in CrCoNi medium-entropy alloy, *Acta Materialia* 240 (2022) 118314. <https://doi.org/10.1016/j.actamat.2022.118314>.
- [62] K. Ming, L. Li, Z. Li, X. Bi, J. Wang, Grain boundary decohesion by nanoclustering Ni and Cr separately in CrMnFeCoNi high-entropy alloys, *Science Advances* 5 (2019) eaay0639. <https://doi.org/10.1126/sciadv.aay0639>.
- [63] A.P. Thompson, H.M. Aktulga, R. Berger, D.S. Bolintineanu, W.M. Brown, P.S. Crozier, P.J. in 't Veld, A. Kohlmeyer, S.G. Moore, T.D. Nguyen, R. Shan, M.J. Stevens, J. Tranchida, C. Trott, S.J. Plimpton, LAMMPS - a flexible simulation tool for particle-based materials modeling at the atomic, meso, and continuum scales, *Computer Physics Communications* 271 (2022) 108171. <https://doi.org/10.1016/j.cpc.2021.108171>.
- [64] A. Stukowski, Visualization and analysis of atomistic simulation data with OVITO—the Open Visualization Tool, *Modelling Simul. Mater. Sci. Eng.* 18 (2010) 015012. <https://doi.org/10.1088/0965-0393/18/1/015012>.
- [65] A. Stukowski, Structure identification methods for atomistic simulations of crystalline materials, *Modelling Simul. Mater. Sci. Eng.* 20 (2012) 045021. <https://doi.org/10.1088/0965-0393/20/4/045021>.
- [66] M.J. McCarthy, H. Zheng, D. Apelian, W.J. Bowman, H. Hahn, J. Luo, S.P. Ong, X. Pan, T.J. Rupert, Emergence of near-boundary segregation zones in face-centered cubic multiprincipal element alloys, *Phys. Rev. Materials* 5 (2021) 113601. <https://doi.org/10.1103/PhysRevMaterials.5.113601>.
- [67] M.A. Tschopp, S.P. Coleman, D.L. McDowell, Symmetric and asymmetric tilt grain boundary structure and energy in Cu and Al (and transferability to other fcc metals), *Integrating Materials* 4 (2015) 176–189. <https://doi.org/10.1186/s40192-015-0040-1>.
- [68] B. Sadigh, P. Erhart, A. Stukowski, A. Caro, E. Martinez, L. Zepeda-Ruiz, Scalable parallel Monte Carlo algorithm for atomistic simulations of precipitation in alloys, *Phys. Rev. B* 85 (2012) 184203. <https://doi.org/10.1103/PhysRevB.85.184203>.
- [69] M. Polak, L. Rubinovich, The competition between surface segregation and compositional ordering in alloys: theory and experimental observations of segregation versus temperature peaked curves, *Colloids and Surfaces A: Physicochemical and Engineering Aspects* 208 (2002) 211–218. [https://doi.org/10.1016/S0927-7757\(02\)00147-4](https://doi.org/10.1016/S0927-7757(02)00147-4).
- [70] W.-R. Jian, L. Wang, W. Bi, S. Xu, I.J. Beyerlein, Role of local chemical fluctuations in the melting of medium entropy alloy CoCrNi, *Applied Physics Letters* 119 (2021) 121904. <https://doi.org/10.1063/5.0064299>.

- [71] R. Darvishi Kamachali, A. Kwiatkowski da Silva, E. McEniry, D. Ponge, B. Gault, J. Neugebauer, D. Raabe, Segregation-assisted spinodal and transient spinodal phase separation at grain boundaries, *Npj Comput Mater* 6 (2020) 1–13. <https://doi.org/10.1038/s41524-020-00456-7>.
- [72] J.M. Cowley, Short- and Long-Range Order Parameters in Disordered Solid Solutions, *Phys. Rev.* 120 (1960) 1648–1657. <https://doi.org/10.1103/PhysRev.120.1648>.
- [73] A. Jarlöv, W. Ji, R. Babicheva, Y. Tian, Z. Hu, H.L. Seet, L. Tan, F. Liu, Y. Liu, M.L.S. Nai, U. Ramamurty, K. Zhou, Tailoring short-range order and dislocation evolution in Cr–Co–Ni medium-entropy alloys: A molecular dynamics study, *Materials & Design* 240 (2024) 112840. <https://doi.org/10.1016/j.matdes.2024.112840>.
- [74] C. Hu, J. Luo, Data-driven prediction of grain boundary segregation and disordering in high-entropy alloys in a 5D space, *Mater. Horiz.* 9 (2022) 1023–1035. <https://doi.org/10.1039/D1MH01204E>.
- [75] T. He, Y. Qi, Y. Ji, M. Feng, Grain boundary segregation-induced strengthening-weakening transition and its ideal maximum strength in nanopolycrystalline FeNiCrCoCu high-entropy alloys, *International Journal of Mechanical Sciences* 238 (2023) 107828. <https://doi.org/10.1016/j.ijmecsci.2022.107828>.
- [76] P. Wynblatt, D. Chatain, Modeling grain boundary and surface segregation in multicomponent high-entropy alloys, *Phys. Rev. Materials* 3 (2019) 054004. <https://doi.org/10.1103/PhysRevMaterials.3.054004>.
- [77] J.L. Hart, A.C. Lang, Y. Li, S. Shahrezaei, D.D. Alix-Williams, M.L. Falk, S.N. Mathaudhu, A.I. Frenkel, M.L. Taheri, Revealing local order via high energy EELS, *Materials Today Nano* 21 (2023) 100298. <https://doi.org/10.1016/j.mtnano.2022.100298>.
- [78] Y. Xia, S. Lyu, W. Li, Y. Chen, A.H.W. Ngan, Defect-induced inhomogeneous atomic environments in complex concentrated alloys, *International Journal of Plasticity* 169 (2023) 103719. <https://doi.org/10.1016/j.ijplas.2023.103719>.
- [79] S. Puri, K. Binder, Surface-directed spinodal decomposition: Phenomenology and numerical results, *Phys. Rev. A* 46 (1992) R4487–R4489. <https://doi.org/10.1103/PhysRevA.46.R4487>.
- [80] R.A.L. Jones, L.J. Norton, E.J. Kramer, F.S. Bates, P. Wiltzius, Surface-directed spinodal decomposition, *Phys. Rev. Lett.* 66 (1991) 1326–1329. <https://doi.org/10.1103/PhysRevLett.66.1326>.
- [81] C. Guo, Y. Gao, Y. Cui, Y. Zhao, C. Xu, S. Sui, X. Wu, Z. Zhang, Phase-field simulation of the spinodal decomposition process near moving grain boundaries, *Materials Today Communications* 35 (2023) 105811. <https://doi.org/10.1016/j.mtcomm.2023.105811>.

- [82] D. Scheiber, T. Jechtl, J. Svoboda, F.D. Fischer, L. Romaner, On solute depletion zones along grain boundaries during segregation, *Acta Materialia* 182 (2020) 100–107. <https://doi.org/10.1016/j.actamat.2019.10.040>.
- [83] Z. Luo, C. Hu, L. Xie, H. Nie, C. Xiang, X. Gu, J. He, W. Zhang, Z. Yu, J. Luo, A highly asymmetric interfacial superstructure in WC: expanding the classic grain boundary segregation and new complexion theories, *Mater. Horiz.* 7 (2020) 173–180. <https://doi.org/10.1039/C9MH00969H>.
- [84] S.-M. Kuo, A. Seki, Y. Oh, D.N. Seidman, Solute-atom segregation: An oscillatory Ni profile at an internal interface in Pt(Ni), *Phys. Rev. Lett.* 65 (1990) 199–202. <https://doi.org/10.1103/PhysRevLett.65.199>.